The Journal of Supercritical Fluids 146 (2019) 1–14

Contents lists available at ScienceDirect

The Journal of Supercritical Fluids

journal homepage: www.elsevier.com/locate/supflu

Modeling hydrocarbon droplet dissolution in near-critical or supercritical water using GCA-EOS and non-ideal diffusional driving force in binary mixtures

Francisco A. Sánchez[a], Ping He[b,c,*], Ahmed F. Ghoniem[c], Selva Pereda[a,d]

[a] Planta Piloto de Ingeniería Química (PLAPIQUI), Chemical Engineering Department, Universidad Nacional del Sur (UNS) - CONICET, Camino La Carrindanga Km 7, 8000B, Bahía Blanca, Argentina
[b] Department of Mechanical Engineering, Lamar University, Beaumont, TX, 77710, United States
[c] Department of Mechanical Engineering, Massachusetts Institute of Technology, Cambridge, MA, 02139, United States
[d] Thermodynamics Research Unit, School of Engineering, University of KwaZulu-Natal, Howard College Campus, King George V Avenue, Durban, 4041, South Africa

GRAPHICAL ABSTRACT

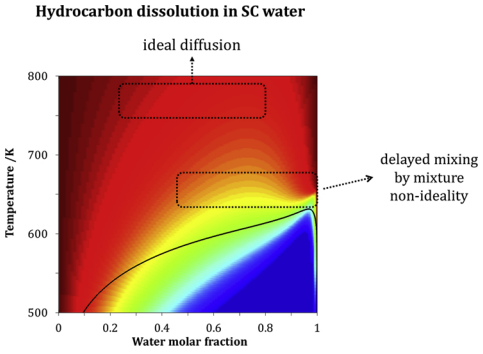

ARTICLE INFO

Keywords:
Non-ideal diffusion
Supercritical water
Hydrocarbons
Thermodynamic properties
Transport phenomena

ABSTRACT

In this work, the mixing of a hydrocarbon droplet in near- and super-critical water (NCW/SCW) is mathematically modeled, coupling thermodynamic properties calculation with transport processes. In non-ideal systems, mass transfer is captured using the generalized Maxwell-Stefan equations with the driving force expressed in terms of the fugacity gradients. The GCA-EOS is used to predict the thermodynamic properties and phase equilibrium compositions. We select *n*-decane, *n*-triacontane, benzene, naphthalene and 1-decylnaphthalene as representative hydrocarbons. Our simulations show delayed mixing processes as the temperature approaches the upper critical solution temperature (UCST) of the mixture, consistent with the impact of non-ideal diffusional driving forces evaluated from pure thermodynamic calculations. Results also show that the phase behavior notably affects the non-ideal driving forces near the UCST, which confirms the importance of coupling accurate thermodynamic models in predictive mixing studies.

* Corresponding author.
E-mail address: phe@lamar.edu (P. He).

https://doi.org/10.1016/j.supflu.2018.12.017
Received 10 October 2018; Received in revised form 21 December 2018; Accepted 21 December 2018
Available online 23 December 2018

List of symbols

A	Helmholtz free energy
ARD(Z)%	Average relative deviation in variable Z: $\frac{100}{N}\sum_i^N \left\|1-\frac{Z_{\text{calc}\,i}}{Z_{\text{exp}\,i}}\right\|$
c_P	Constant pressure heat capacity
D_{ij}	Binary diffusion coefficient
D_i^T	Thermal diffusion coefficient
$\tilde{d}$	Coefficient of driving force
d_i	Effective hard sphere diameter of component i
d_{ci}	Effective hard sphere diameter of component i evaluated at T_c
G	Gibbs energy
g_j	Group energy per surface segment of group j
H	Total enthalpy
HC	Hydrocarbon
H	Molar enthalpy
J_i	Radial mass flux of component i
K_i	Partition coefficient of component i
LLE	Liquid-liquid equilibria
M_i	Total number of associating sites in group i
$\dot{m}$, $\dot{m}_i$	Total and component mass fluxes at the interface.
NEq	Number of experimental equilibrium points
NC	Number of components in the mixture
NG	Number of attractive groups in the mixture
NGA	Number of associating groups in the mixture
P	Pressure
q_j	Number of surface segments of group j
R	Universal gas constant
r	Radial distance in spherical coordinates
T	Temperature
T_{ci}	Critical temperature of component i
t	Time
t_W	Water diffusion time
$\tilde{t}_W$	Normalized water diffusion time
u	Radial speed
UCEP	Upper critical end point
UCST	Upper critical solution temperature
V	Total volume of the mixture
VLE	Vapor-liquid equilibria
w_i	Mass composition of component i
X_{ki}	Fraction of non-bonded associating sites of type k in group i
x_i	Molar composition in liquid phase of component i
y_i	Molar composition in vapor phase of component i
z	Coordination number

Greek symbols

α_{ij}	Non-randomness parameter between groups i and j
ε_{kilj}	Energy of association between site k of group i and site l of group j
κ_{kilj}	Volume of association between site k of group i and site l of group j
λ	Thermal conductivity
μ	Viscosity
μ_i	Chemical potential of compound i
ν_{ij}	Number of groups j in compound i
ν_{ij}^*	Number of associating groups j in compound i
$\hat{\varphi}_i$	Fugacity coefficient of compound i in the mixture

1. Introduction

Supercritical fluid (SCF) technologies, such as supercritical fluid extraction, supercritical water oxidation, supercritical water reforming and gasification, etc., show advantages because of the singular physicochemical properties exhibited in SCFs. Because of the strong coupling of thermodynamics, transport phenomena, and chemical kinetics (for reacting systems), modeling high pressure operating units has been a continuing challenge in this field. Mass transfer models are normally based on the Fick's law or the Maxwell-Stefan (MS) expressions. Curtiss and Bird [1] proved that the generalized forms of the Fick's law and the MS expressions were equivalent, giving the same relation that defines the dependency of the mass flux on the diffusive driving forces but in different forms. Nonetheless, MS expressions are simpler in multicomponent systems. The driving forces can be calculated using the ideal fluid assumption, that is $-c\nabla x_i$ (where c is the concentration, and x_i is the mole fraction of species i). This ideal driving force has been commonly used in diffusion studies. However, when non-ideal fluid behavior becomes important, Krishna et al. [2] proposed, without derivation, a formulation of the non-ideal diffusive driving force. Recently, Bird et al. [1,3] re-derived the same formulation based on a thorough theoretical analysis using the molecular theory of gases and liquids (MTGL) [4]. The non-ideal driving force depends not only on the concentration gradient, but also on the gradients of partial fugacities.

Most prior studies [5–16] used the ideal fluid model to compute the diffusive driving force, while the mixture non-ideality was taken into account only in the equation of state, thermodynamic and transport properties. On the other hand, the following studies used the non-ideal driving force for SCF mixtures: Werling and Debenedetti [17,18] studied the mixing of a toluene droplet with supercritical CO_2. Bellan et al. modeled the mixing of H_2 and O_2 [19–22], and heptane and N_2 [23], in which the fluctuation theory was used to calculate the mass and heat fluxes from a transport matrix [24]. The fluctuation theory is a generalized Fick's law approach, which is equivalent to the generalized MS approach. The derivations were documented in MTGL [4], and a recent review by Curtiss and Bird [1], confirms that the MS approach is easier to apply to multicomponent mixtures because the coefficients are independent of the concentration. In contrast, the two approaches are the same in binary mixtures.

Studies using the non-ideal driving force show that the importance of considering the non-ideality of the system has been underestimated. Our previous work [10–13,25] on mixing of a hydrocarbon (HC) droplet in NCW/SCW using the ideal driving force revealed that the non-ideal thermodynamic properties, e.g. the upper critical solution temperature (UCST), played an important role in the mixing process. Recently, we explored the impact of the non-ideal diffusion on the binary and multicomponent mixing of hydrocarbons and NCW/SCW, and we found that the non-ideal diffusion largely increases the mixing time, compared to the case with the ideal diffusion, when approaching the UCST [26]. For heavy hydrocarbons in water, e.g., 1-decylnaphthalene and 1-decylnaphthalene + benzene, the mixing times predicted using the non-ideal diffusion model were over twice the time predicted by the ideal diffusion model [26]. In addition, in our more recent mathematical modeling work [27], we predicted phase separation of light HC and heavy HC because of the non-ideal diffusion during the mixing of a binary HC droplet in NCW/SCW.

In this paper, we analyze in detail the effect of the critical point proximity using the Group Contribution Equation of State (GCA-EOS) [28,29] to account for the mixture non-ideality in the total driving forces. This model predicts qualitatively the mutual solubilities and critical loci of water + hydrocarbons mixtures. Furthermore, for mono- and poly-cyclic aromatic compounds studied [29,30], we showed that the model is able to predict the correct type of phase behavior of different water + aromatic HC binary mixtures, as defined by Konynenburg and Scott [31]. On the other hand, the interaction parameters between paraffinic groups and water have been revised to improve the

correlation of the phase behavior near the critical loci of water + *n*-alkane binary mixtures. Finally, the results achieved with GCA-EOS are compared with those obtained with the classical cubic Peng-Robinson (PR)-EOS.

2. Physical problem, governing equations and numerical methods

2.1. Physical problem

The model problem examined in this work consists of a HC droplet placed in a reservoir of near- or super-critical water. We assumed spherical symmetry to model the mass transfer out of the dissolving droplet. Moreover, the radial velocity of the droplet interface is non-zero because of the thermal expansion and the diffusion between the water-rich and HC-rich phases. Since mixing timescales are on the order of seconds [10,11,26,32], while under the conditions modeled here, the kinetics timescales of HC pyrolysis are on the order of minutes to hours [33–36], chemical reactions are neglected in this mixing study.

2.2. Governing equations

The governing equations of the mixing process are the mass, momentum, species, and energy conservation laws in 1-D spherical coordinates, and the equation of state:

$$\frac{\partial \rho}{\partial t} + \frac{1}{r^2}\frac{\partial}{\partial r}(r^2 \rho u) = 0 \tag{1}$$

$$\frac{\partial \rho u}{\partial t} + \frac{1}{r^2}\frac{\partial}{\partial r}(r^2 \rho u^2) = -\frac{\partial P}{\partial r} + \frac{1}{r^2}\frac{\partial}{\partial r}(r^2 \tau_{rr}) - \frac{1}{r}(\tau_{\theta\theta} + \tau_{\phi\phi}) \tag{2}$$

$$\frac{\partial \rho w_i}{\partial t} + \frac{1}{r^2}\frac{\partial}{\partial r}(r^2 \rho w_i u) = -\frac{1}{r^2}\frac{\partial}{\partial r}(r^2 J_i) \tag{3}$$

$$\rho c_P \frac{\partial T}{\partial t} + \rho c_P u \frac{\partial T}{\partial r} = \frac{1}{r^2}\frac{\partial}{\partial r}\left(r^2 \lambda \frac{\partial T}{\partial r}\right) - \sum_i \frac{\partial \bar{h}_i}{\partial r}\frac{J_i}{M_i} \tag{4}$$

where ρ, u, P, w_i, J_i, and T are the density, radial velocity, pressure, mass fraction of species i, radial mass flux of species i, and temperature; in addition, c_P, λ, and M_i are the specific heat, thermal conductivity, and molecular weight, respectively. $\bar{h}_i = (\partial H/\partial n_i)_{T,P,n_{j\neq i}}$ is the partial molar enthalpy, H, the total enthalpy and n_i is the number of moles of species i. The temporal and spatial coordinates are represented by t and (r, θ, ϕ). The shear stress components are given by

$$\tau_{rr} = \frac{4}{3}\mu\left(\frac{\partial u}{\partial r} - \frac{u}{r}\right), \quad \tau_{\theta\theta} = \tau_{\phi\phi} = -\frac{2}{3}\mu\left(\frac{\partial u}{\partial r} - \frac{u}{r}\right) \tag{5}$$

The equation of state used in this study (GCA-EOS) is presented in Section 3, from which the partial molar enthalpies are computed.

2.2.1. Multicomponent mass transfer

The radial mass flux J_i is governed by the Maxwell-Stefan equations [1]:

$$\sum_{j=1,j\neq i}^{NC} \frac{x_i x_j}{D_{ij}}\left(\frac{J_j}{\rho w_j} - \frac{J_i}{\rho w_i}\right) = d_i - \sum_{j=1,j\neq i}^{NC} \frac{x_i x_j}{D_{ij}}\left(\frac{D_j^T}{\rho w_j} - \frac{D_i^T}{\rho w_i}\right)\ln T \tag{6}$$

where *NC* stands for the number of components, x_i is the mole fraction of species i, D_{ij} is the binary diffusion coefficient, D_i^T is the thermal diffusion coefficient, and d_i is the diffusive driving force in the radial direction. Note that the thermal diffusion term in Eq. (6) is neglected based on a quantitative analysis in one of our previous papers [27]. Although the temperature gradient is relatively large at the early stage of mixing, the mass flux due to thermal diffusion for hydrocarbons calculated based on experimental data [37,38] is much smaller than that by chemical potential gradients (for more details, see Supplementary Material in [27]). Therefore, the driving force [1–3] is:

$$d_i = \frac{x_i}{R\,T}\left(\frac{\partial \mu_i}{\partial r}\right)_{T,P} \tag{7}$$

where μ_i is the chemical potential of species i. Applying the chain rule and taking into account spherical symmetry,

$$d_i = \frac{\partial x_i}{\partial r} + x_i \sum_{j=1}^{NC}\left[n\left(\frac{\partial \ln \hat{\varphi}_i}{\partial n_j}\right)_{T,P,n_{k\neq j}}\right]\frac{\partial x_j}{\partial r} \tag{8}$$

where $\hat{\varphi}_i$ is the fugacity coefficient, and its derivatives are calculated from the EOS, and n is the total number of moles. Eq. (8) formulates the non-ideal diffusive driving force, whose second term represents the non-ideality in the mixture, reduced to the ideal driving force, when $\hat{\varphi}_i \equiv 1$ for ideal gas mixtures:

$$d_i = \frac{\partial x_i}{\partial r} \tag{9}$$

2.2.2. Jump conditions across the phase interface

The interface between partially miscible fluids propagates at speed u_s, which is determined by the mass and species balance across the interface

$$\dot{m} = \rho_1(u_1 - u_s) = \rho_2(u_2 - u_s) \tag{10}$$

$$\dot{m}_i = \rho_1(u_1 - u_s)w_{1,i} + J_{1,i} = \rho_2(u_2 - u_s)w_{2,i} + J_{2,i} \tag{11}$$

where "1" denotes the left side of the interface and "2" the right side; $\dot{m}_i$, and $\dot{m}$ are the mass flux of species i, and net flux across the interface, respectively. The temperature profile across the interface, T, is continuous; however, its gradient is not. On the other hand, the temperature at the interface, T_s, is determined from the energy balance assessed at the interface

$$-\lambda_1(\nabla T)_1 = -\lambda_2(\nabla T)_2 + q^* \tag{12}$$

where $q^* = \sum_i \dot{m}_i/M_i(\bar{h}_{2,i} - \bar{h}_{1,i})$, $\bar{h}_{1,i}$ is the partial molar enthalpy on the left side of the interface, and $\bar{h}_{2,i}$ on the right side. The mass fractions on both sides of the phase interface, $\{w_{1,i}\}$ and $\{w_{2,i}\}$, are taken as the equilibrium compositions according to the isofugacity criteria

$$\hat{f}_{1,i} = \hat{f}_{2,i} \ \text{ or } x_{1,i}\,\hat{\varphi}_{1,i} = x_{2,i}\,\hat{\varphi}_{2,i} \tag{13}$$

It is worth noting that the isofugacity criteria and species balance are uncoupled in binary systems. However, they are not independent in multicomponent systems [32].

2.2.3. Boundary conditions

Neumann and Dirichlet boundary conditions are applied at the end of the domain (denoted by "ED"), i.e. $(\partial u/\partial r)|_{ED} = 0$, $(\partial w_i/\partial r)|_{ED} = 0$, and $T|_{ED} = T_{W,0}$. Spherical symmetry is enforced at the center of the droplet (denoted by "CD"), i.e. $u|_{CD} = 0$, $(\partial w_i/\partial r)|_{CD} = 0$, and $(\partial T/\partial r)|_{CD} = 0$. The droplet initial temperature is $T_{H,0}$, which is fixed in this study at 373 K, and initial compositions are $\{w_{H,0} = 1,\ w_{W,0} = 0\}$ in the HC droplet, and $\{w_{H,0} = 0,\ w_{W,0} = 1\}$ in water, where the subscript "H" denotes the HC and "W" water. The water reservoir has an initial temperature of $T_{W,0}$. The same temperature is used as the boundary condition at ED. Different values of $T_{W,0}$ have been tested in this study. A schematic representation of the simulation geometry is shown in Fig. 1.

2.2.4. Physical properties

The Tracer Liu–Silva–Macedo (TLSM) equation [39] is used to compute tracer binary diffusion coefficients, and Wesselingh and Krishna model [40] is used to construct binary diffusion coefficients based on the tracer values. Moreover, Chung's method [41] is used to calculate the viscosity and thermal conductivity. The critical constants (P_c, T_c, and v_c), acentric factor ω, dipole moment, and association parameter of molecules assessed in this study are obtained from *Yaws' Handbook* [39].

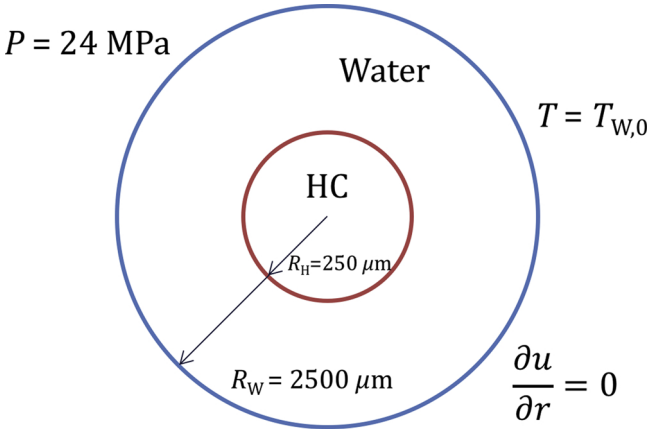

Fig. 1. Simulation geometry scheme.

2.3. Numerical methods

In a previous work, we proposed a sharp interface method using mixed finite difference/volume approach to model the mixing of partially miscible fluids [27]. The same method is used in this paper. A summary of our method is presented here, and we refer interested readers to reference [27] for the details. Euler's method is used to integrate the equations in time. A standard staggered uniform grid is used, where the mass and heat fluxes are defined on the cell faces and all other variables are defined at the cell centers. A second-order central difference scheme is used to discretize partial derivatives for bulk cell faces, while, for the interfacial cell faces, a third order smooth, mixed one-sided finite difference scheme with variable grid size according to the location of the interface is used to compute the partial derivatives. A standard finite volume method is applied to integrate the transport equations in bulk cells, while, an irregular finite volume method with a variable distance according to the interface location is implemented at the interfacial cells. An iterative solver for the coupled phase equilibrium (Eq. 13) and transport constraints (Eqs. 10–12) is used to compute the compositions on both sides of a phase interface, and a novel algorithm to capture the formation of a new interface [27]. Our model has been validated in one of our previous papers [32] through comparisons with simulations of evaporating binary and ternary droplets in the literature.

The mixing of an HC droplet, whose radius is 250 μm, in NCW/SCW at 24 MPa and at different water bath temperatures, $T_{W,0}$ is modeled. In all cases, the HC droplet is initially at $T_{H,0}$ = 373 K, and at the same P as water. The water domain extends to r = 1 mm. The simulations presented in this paper use a grid size of $\Delta r = 2\,\mu$m. In addition, a dynamic time stepping is used, given by a Courant number of 0.1. Grid size and time-step independence have been tested in [32].

3. Thermodynamic modeling

3.1. The Group Contribution with Association Equation of State (GCA-EOS)

The GCA-EOS [28] is an extension of the original GC-EOS [42] to associating systems, which is based on the Generalized van der Waals theory. There are three contributions to the residual Helmholtz energy (A^R) in the GCA-EOS model: free volume (A^{fv}), attractive (A^{att}) and association (A^{assoc}):

$$A^R = A^{fv} + A^{att} + A^{assoc} \tag{14}$$

The *free volume* contribution is the extended Carnahan-Starling [43] equation for mixtures of hard spheres developed by Mansoori et al. [44], which is characterized by one pure-compound parameter: the critical diameter (d_c). The *attractive* contribution to the residual Helmholtz energy, A^{att}, accounts for dispersive forces between functional groups. It is a van der Waals expression combined with a density-dependent, local-composition mixing rule based on a group contribution version of the NRTL model [45]. This term is characterized by the number of surface segments of each group (q), and the surface energy (g), which is temperature dependent. Furthermore, each binary group interaction is characterized by one interaction parameter ($k_{ij} = k_{ji}$), which may or may not be temperature dependent, and two binary damping factors ($\alpha_{ij} \neq \alpha_{ji}$). Finally, the *association* term, A^{assoc}, is a group contribution version of the SAFT equation developed by Chapman et al. [46]. This term is characterized by two parameters: the energy ($\varepsilon_{ki,lj}$) and volume ($\kappa_{ki,lj}$) of association. Naturally, the latter term will only be present in the case of components showing specific association interaction (hydrogen-bonding or solvation). A list of GCA-EOS parameters is shown in Table 1. A more detailed explanation of the model can be found in Appendix A.

3.2. GCA-EOS performance for water + hydrocarbon binary mixtures at high pressure and temperature

As mentioned previously, Sánchez et al. [29] showed that the GCA-EOS is adequate for predicting both, the mutual solubility and critical locus of water + aromatic hydrocarbon binary mixtures. Moreover, Sánchez [30] showed that the GCA-EOS is able to predict the correct

Table 1
GCA-EOS parameters.

Contribution	Parameter			Attribute
Free-volume[a]	Pure compound	Hard sphere diameter	d_c	Fixed[c]
		Critical temperature	T_c	Fixed
Attractive[b]	Pure group	Reference temperature	T_i*	Fixed
		Surface area	q_i	Fixed[d]
		Energy[d]	g_{ii}*,g_{ii}',g_{ii}''	Adjustable[e]
	Binary	Energy interaction[e]	k_{ij}*, k_{ij}'	Adjustable[e]
		Non-randomness	α_{ij} α_{ji}	Adjustable
Associating[b]	Pure group	Self-association energy	$\varepsilon_{ki\text{-}ki}$	Fixed
		Self-association volume	$\kappa_{ki\text{-}ki}$	Fixed
	Binary	Cross association energy	$\varepsilon_{ki\text{-}lj}$	Comb.rule/Adjustable[e,f]
		Cross association volume	$\kappa_{ki\text{-}lj}$	Comb.rule/Adjustable[e,f]

[a] Molecular term.
[b] Group contribution term.
[c] Calculated from critical point conditions for molecular compounds, density or vapor pressure data for compounds described by GC.
[d] Value taken from Bondi [47]. In certain cases, this parameter can be adjustable if it is not available.
[e] See Ref. [48,49] for details.
[f] For groups that can only cross associate, these parameters are fitted to binary data.

type of phase behavior of aromatic compounds. In this regard, Fig. 2 compares the experimental critical loci and three phase lines for binary systems of water + benzene or naphthalene calculated using the software GPEC [50]. As can be seen, the model is able to predict with a fair degree of accuracy the UCST and also the type of phase behavior for this mixture. It overestimates the UCST at 24 MPa by approximately 15 K and 5 K for benzene and naphthalene binaries, respectively, which is still acceptable. Furthermore, pure naphthalene critical point is slightly underestimated, although this is related to the pure AC group parameters, q_{AC} and g_{AC}, reported in the original GC-EOS work [51], and not to the binary interaction parameters. In summary, the GCA-EOS predicts qualitatively well both binaries phase behavior and reparameterization of pure groups is beyond the scope of this work.

On the other hand, the interaction parameters between H_2O and aliphatic groups (CH*x*) provided by Soria et al. [52] reproduce correctly the mutual solubility, though the critical locus reproduction is less satisfactory. Consequently, based on the premise of this work, we revisit the interaction parameters between H_2O and CH*x* groups in order to improve the reproduction of the critical loci in the vicinity of the water critical point.

3.3. Parameterization procedure

The parameterization procedure was performed through the optimization of the following objective function:

$$\text{O. F.} = \sum_{i=1}^{NEq} e_{\text{eq},i}^2 \tag{15}$$

where *NEq* are the number of binary equilibrium points, and $e_{\text{eq},i}$ is the corresponding error between experimental and calculated data point as follows:

$$e_{\text{eq},i}^2 = \left(\frac{x_{\text{exp},i} - x_{\text{calc},i}}{x_{\text{exp},i}}\right)^2 + \left(\frac{y_{\text{exp},i} - y_{\text{calc},i}}{y_{\text{exp},i}}\right)^2 \tag{16}$$

where *x* and *y* are the molar fraction in the liquid and vapor phase, respectively. During the parameterization procedure, all binary vapor-liquid equilibria (VLE) and liquid-liquid (LLE) data were evaluated through *TP* flash calculation [54,55]. The objective function (Eq. 15) was minimized upon the Levenberg–Marquardt algorithm of finite difference coded in Fortran77.

The data included in the parameterization comprises near critical VLE-LLE of water + *n*-dodecane at 633 K [56], and water solubility in *n*-hexadecane and *n*-eicosane [57]. This is done in order to obtain a good description of the critical locus of *n*-alkanes, while keeping a reasonable description of the mutual solubility. A detailed list of all GCA-EOS parameters used in this work gathered from the literature is shown in Appendix B.

4. Results and discussion

4.1. High pressure and temperature phase equilibria of alkane + H_2O binary mixtures

Studies performed in this work require a sufficiently precise reproduction of the mutual solubility and critical locus, simultaneously. To assess this kind of phase behavior, a parameter fitting was performed of water + selected alkanes. Parameterization results of water + aliphatic HC binary systems are presented in Table 2. It is worth mentioning that only the binary interaction parameters of H_2O with CH_3^∞ or CH_2^∞ groups were revisited, while the corresponding aromatic groups (ACH^∞, AC^∞ and $ACCH_2^\infty$) were taken from previous work [29]. Fig. 3 depicts graphically the resulting parameterization at 633 K, where it is also shown that the phase behavior is also extrapolated with a similar quality to $T = 604$ K. Moreover, Fig. 4 shows the calculation of the *PT* projection of the phase equilibria of water + selected *n*-alkanes. As can be seen, the performed parameterization allows accurately reproducing the critical loci of water + *n*-decane and + *n*-eicosane. On the other hand, the critical temperatures of water + *n*-triacontane system are overestimated by approximately 10 K; nonetheless, this result is still acceptable. Furthermore, the model is able to predict the transition between Types IIIa (critical locus starting from the compound with larger P_c diverges) and IIIb (critical locus starting from the compound with lower P_c diverges) between *n*-eicosane and *n*-triacontane.

4.2. Hydrocarbon droplet dissolution in NCW and SCW

As discussed in [26], the non-ideal model captures a strong barrier resisting water diffusion into the HC-rich phase. The strong diffusion barrier against water diffusion is captured independently by the mixing simulations and pure thermodynamic calculations. A normalized water diffusion time is used to quantify the effect of diffusion barrier in the mixing simulations, where the thermodynamics and transport phenomena are tightly coupled; and a departure coefficient of diffusive driving force (Eq. 19) is used to quantify the same effect using pure thermodynamic calculations. Both quantities have been found consistent in this study and will be presented in next sections.

4.2.1. The water diffusion time

The water diffusion time, t_W, is defined as the time required for reaching an 80% of the equilibrium water molar fraction at the center of the droplet. In our previous work, using PR-EOS [26], we showed that both driving force models (Eqs. 8 and 9) lead to similar results when $T_{W,0}$ is below the UCST (at the same pressure). On the other hand, when $T_{W,0}$ is near and above UCST, the mixing predicted using the non-ideal driving force (Eq. 8) was significantly delayed. Likewise, the predictions obtained using the GCA-EOS follows the same tendency, as illustrated in Fig. 5 for benzene. When $T_{W,0}$ approaches the UCST, water diffusion time increases because more water can diffuse into the HC droplet. In this case, when water temperature reaches the UCST, both the ideal and non-ideal models predict a sudden increase in the water diffusion time, but the non-ideal model predicts a larger jump. As $T_{W,0}$ increases above the UCST, the water diffusion time decreases. This is because the temperature at the interface reaches the UCST more quickly. Also, the difference between the ideal and non-ideal cases becomes smaller, because the non-ideal effect tends to disappear at higher temperatures.

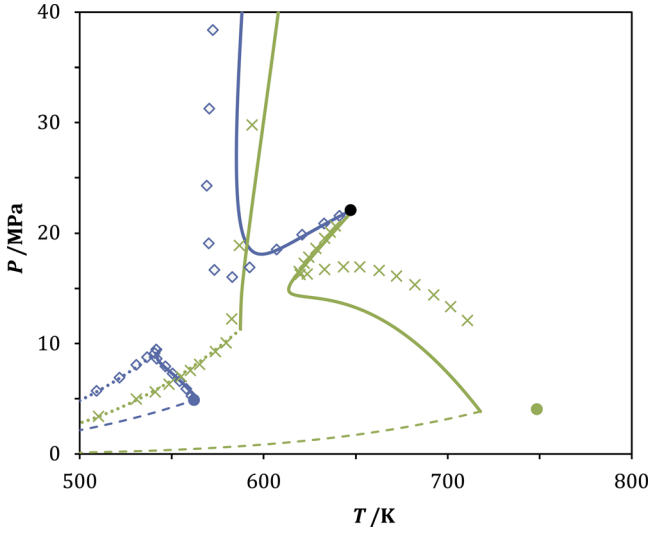

Fig. 2. *PT* projection of the phase equilibria of H_2O + aromatic hydrocarbons. Symbols: experimental data [53] for (◇) benzene and (×) naphthalene. Filled circles: pure compound critical point. Lines: GCA-EOS prediction of: (- - -) pure vapor pressures, (—) critical loci, and (· · ·) three phase line.

Table 2
Binary interaction parameters regressed in this work.

Group		k_{ij}*	k_{ij}'	α_{ij}	α_{ji}
i	*j*				
H_2O	CH_3^{∞}	0.6723	−0.055	−7.704	0.691
	CH_2^{∞}	0.5013	−0.075	−4.549	8.218

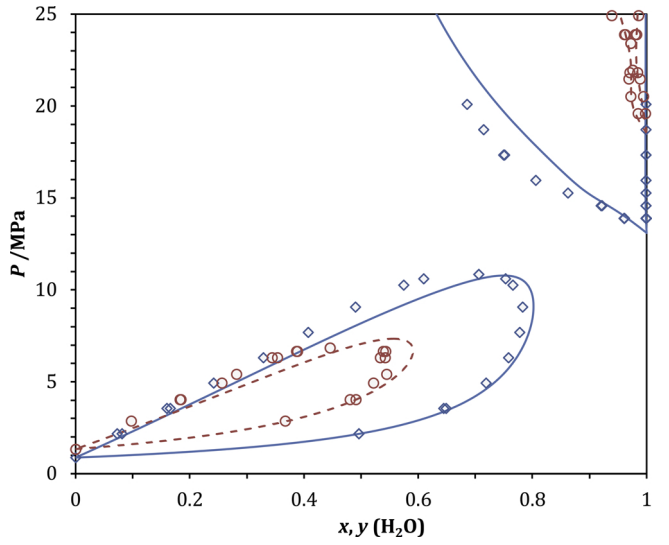

Fig. 3. High pressure phase equilibria of water + *n*-dodecane. Symbols: experimental data [56] at (◇) 604 and (O) 633 K. Dashed and solid lines: GCA-EOS correlation and prediction, respectively.

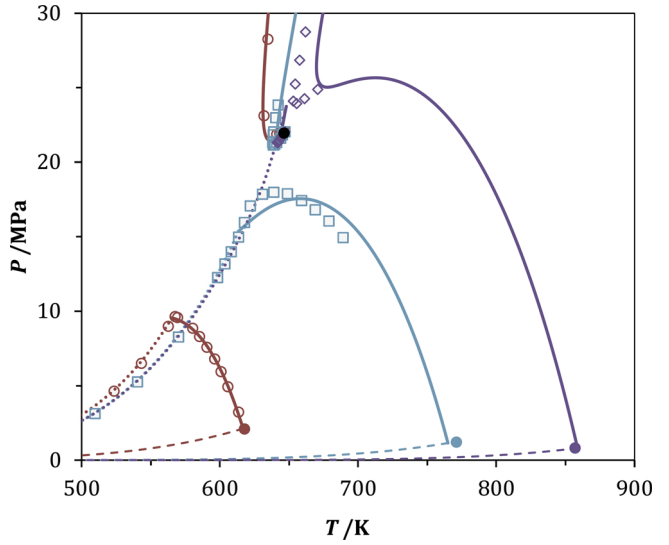

Fig. 4. *PT* projection of the phase equilibria of H_2O + *n*-alkanes. Symbols: experimental data [58] for (O) *n*-decane, (□) *n*-eicosane, and (◇) *n*-triacontane; filled circles: pure compound critical point. Lines: GCA-EOS predictions of: (- - -) pure vapor pressures, (—) critical loci, and (· · ·) three phase lines.

The non-ideality of mixing can be evaluated by means of the *normalized diffusion time* defined as:

$$\tilde{t}_W = \frac{t_{W,non-ideal}}{t_{W,ideal}} \tag{17}$$

where the difference from unity indicates the effect of non-ideal diffusion. Fig. 6 depicts the results for the five model HCs studied in this work. As shown, $\tilde{t}_W > 1$ at all temperatures, while it reaches a maximum slightly after the UCST. Furthermore, the maximum $\tilde{t}_W$ varies between 1.5 for *n*-triacontane and 2.4 for naphthalene.

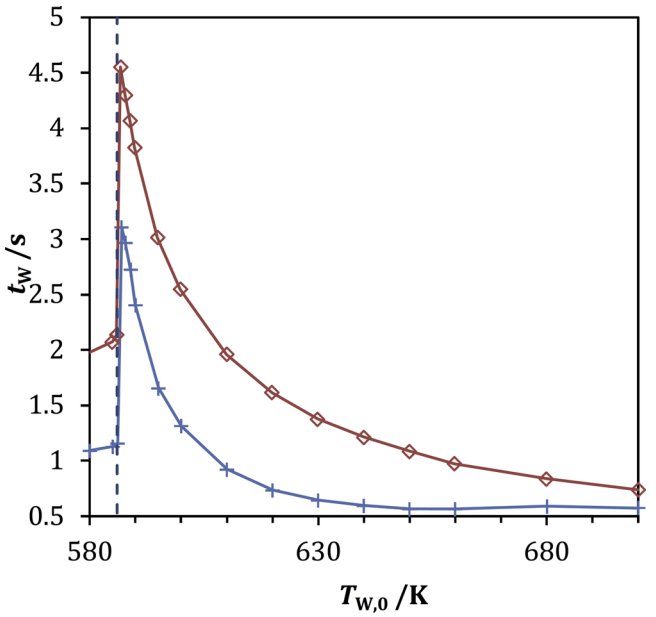

Fig. 5. Water diffusion times for mixing of a benzene droplet, with water at different initial water temperatures, $T_{W,0}$, using ideal (+) and non-ideal (◇) diffusive driving forces (the dashed vertical line shows the UCST at 24 MPa).

Fig. 6 shows that $\tilde{t}_W$ is continuous for *n*-decane and 1-decylnaphthalene across the UCST, while it is discontinuous for other species. The jump of $\tilde{t}_W$ is caused by the jump of water solubility in the HC-rich phase, x_W, across the UCST, as x_W, jumps from its value at UCST to unity immediately above UCST. If x_W at UCST is close to 1, there is no jump of x_W at UCST; otherwise, there is a distinct jump. The larger the jump of x_W is, the larger the jump of $\tilde{t}_W$ becomes.

4.2.2. The departure coefficient of the diffusive driving force

Alternatively, the effect of the non-ideality on the driving force can be analyzed by comparing Eqs. (8) and (9). When applied to binary mixtures, the driving force can be written as:

$$d_{HC} = \tilde{d}\,\frac{\partial x_{HC}}{\partial r} \tag{18}$$

where $\tilde{d}$ is the *departure* coefficient of the driving force, and is defined as:

$$\tilde{d} = \frac{x_{HC}}{RT}\left(\frac{\partial \mu_{HC}}{\partial x_{HC}}\right)_{T,P} = 1 + x_{HC}\left[n\left(\frac{\partial \ln \hat{\varphi}_{HC}}{\partial n_{HC}}\right)_{T,P,n_W} - n\left(\frac{\partial \ln \hat{\varphi}_{HC}}{\partial n_W}\right)_{T,P,n_{HC}}\right] \tag{19}$$

At a fixed pressure and for a binary mixture, this parameter depends only on the molar fraction of one compound and temperature. The derivatives of the fugacity coefficient with respect to concentrations are the primary contributors to the departure of the driving force from the ideal case, whose effect is stronger near the UCST. This influence can be easily explained by means of the critical conditions of the binary mixture [59]:

$$\left(\frac{\partial \mu_1}{\partial x_1}\right)_{T_c,P_c} = \left(\frac{\partial^2 \mu_1}{\partial x_1^2}\right)_{T_c,P_c} = 0;\ \left(\frac{\partial^3 \mu_1}{\partial x_1^3}\right)_{T_c,P_c} > 0 \tag{20}$$

Hence, because $\tilde{d} = 0$ at the UCST, the non-ideal diffusion model predicts delayed mixing. This effect is visualized in Fig. 7, where the values of $\tilde{d}$ are shown in a contour plot as function of the water molar fraction and temperature. Furthermore, Fig. 7 shows the mutual solubility predicted by the GCA-EOS as a black line for all four HCs studied in this work. The experimental data of Haruki et al. [57] are also shown

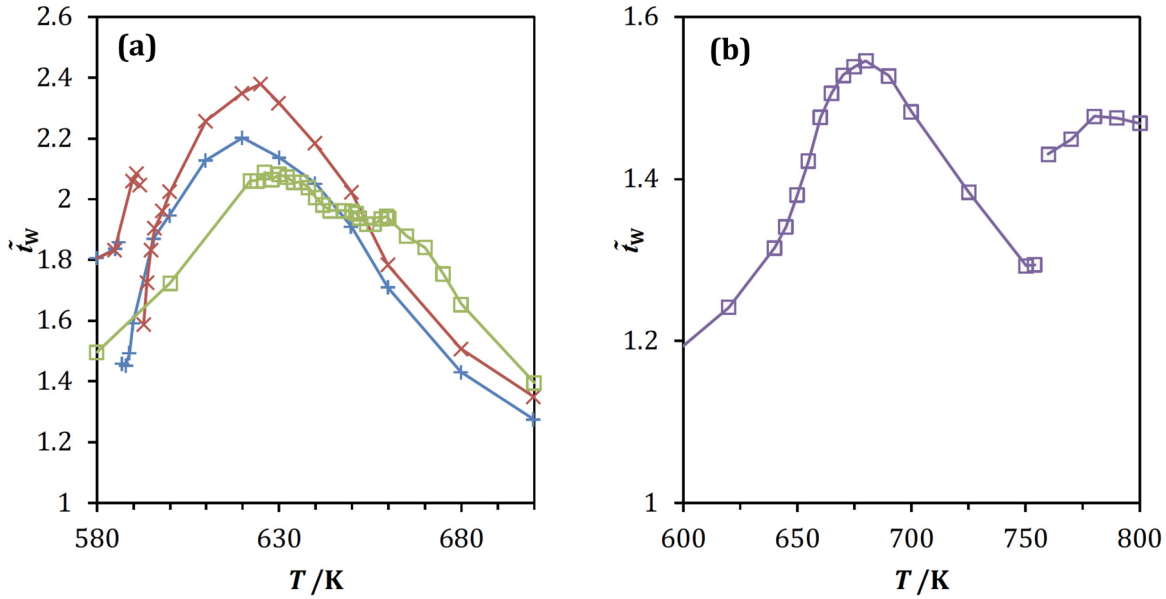

Fig. 6. Normalized mixing time, $\tilde{t}_W$, of the binary systems under stady at 24 MPa and different T_{W0} values. Symbols: simmulation data for (a) (+) benzene, (×) naphthalene, (□) *n*-decane, (O) 1-decylnaphthalene, and (b) (◇) *n*-triacontane (The lines are meant only as a guide to the eye).

for *n*-decane + water binary for comparison. Additionally, the *Tx* projection of the critical lines for each binary system are shown as a thick violet line. It is worth noting that the critical lines of each binary system are not at constant pressure, as evident from Figs. 2 and 4. Moreover, Fig. 7d shows a peculiar behavior of the mutual solubility of water + *n*-triacontane binary mixture. Nonetheless, this behavior is simply due to the fact that this system exhibits VLE up to pressures of 25.6 MPa, according to GCA-EOS predictions in Fig. 4.

In Fig. 7, the phase envelope marks the single-phase and two-phase regions: the single-phase region is outside the envelope; and the two-

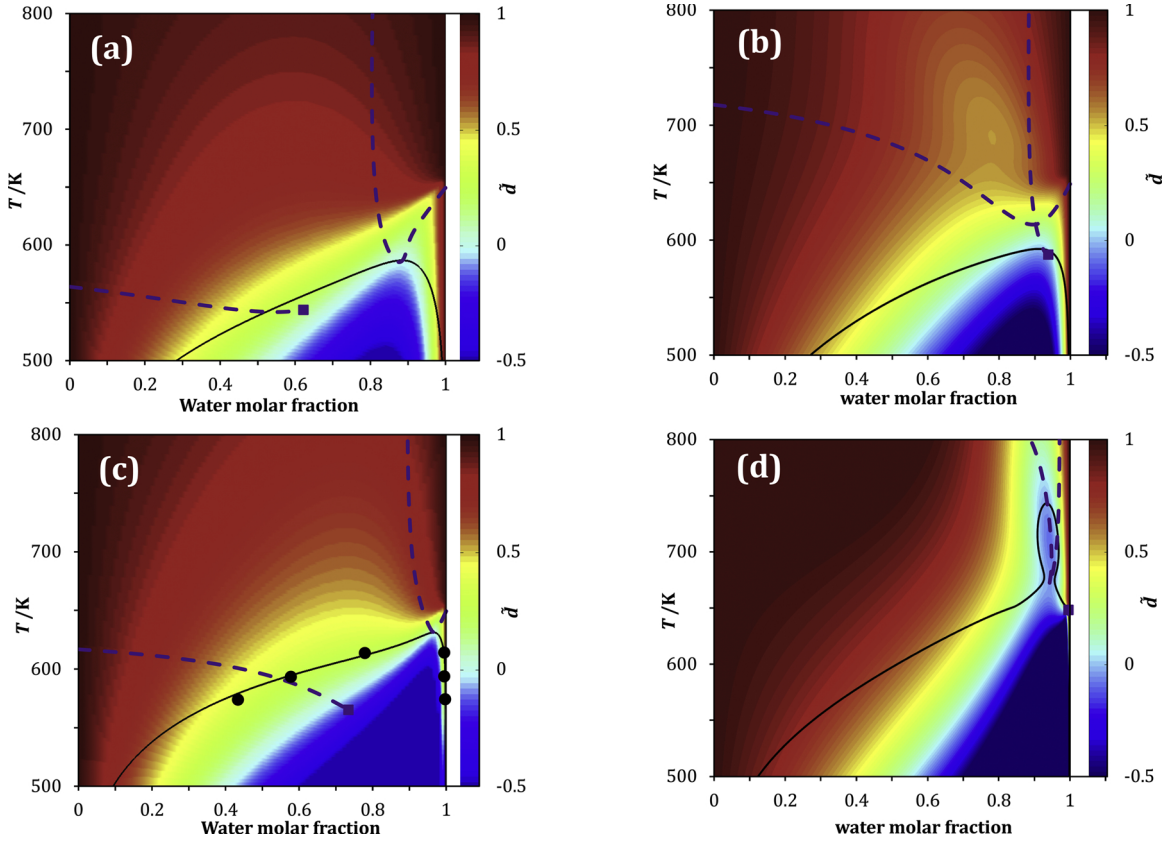

Fig. 7. Departure coefficient of the driving force, $\tilde{d}$, contour chart for model HC + H_2O binary systems at 24 MPa from the GCA-EOS. Black circles: experimental mutual solubility data. Black solid lines: mutual solubility at 24 MPa calculated with the GCA-EOS. Thick violet dashed lines: *Tx* projection of the critical loci predicted by the GCA-EOS; violet square: predicted critical end-point. (a) benzene; (b) naphthalene; (c) *n*-decane; (d) *n*-triacontane. (For the color reference of $\tilde{d}$, the reader is referred to the electronic version of this article.).

phase region is inside. There are sub-regions with negative and positive $\tilde{d}$ in the two-phase region. Because $\tilde{d}$ in the two-phase region does not affect mass transfer in the bulk, the non-ideal diffusion process is only influenced by $\tilde{d}$ in the single-phase region. In addition, the sharp interface method used in this paper explicitly describes the phase interface as a jump condition. Thus, only the single-phase region, also called the miscible region, is discussed in the following.

Fig. 7 clearly shows that $\tilde{d}$ is zero at the UCST, which indicates that mixing is significantly delayed near the UCST region. On the other hand, $\tilde{d}$ tends to unity at higher temperatures, and at lower temperatures within the miscible region, which indicates that mixing tends to be ideal. However, it is also shown that there are some regions where $\tilde{d}$ is largely reduced from unity, as shown from green to orange in the *Tx* plane. The driving force is decreased *near* the critical points, and the curve of the critical lines closely follows the shapes of the contour of the departure coefficient. The non-ideal region above the phase envelope can be defined as the area where $\tilde{d}$ is less than unity. The wider the non-ideal region is, the stronger the non-ideal effect is.

Figs. 6 and 7 show that the non-ideal effect tends to be slightly stronger for systems containing aromatic HCs. These systems have the lowermost UCST, and therefore the non-ideal phase behavior effect is stronger right after the UCST of the corresponding HC-water binaries. The correspondence between the phase behavior and non-ideal diffusion for each binary system under study here are discussed in the following:

1) Water + benzene system (Fig. 7a) exhibits a strong non-ideal effect. The critical locus starting from the water critical point extends down to lower temperatures than other cases. This causes the non-ideal region to grow from very close to the water critical point up to the UCST. However, because the *Tx* projection of the same critical locus does not expand too much in the *x*-coordinate (stops at ~ around $x = 0.8$), the non-ideal region does not grow towards $x = 0$. Moreover, the critical locus beginning from the benzene critical point starts at a lower temperature than that of water + naphthalene but at the same time it covers much lower pressures than 24 MPa. Although the overall non-ideal region of water + benzene is somewhat smaller than that of water + naphthalene at higher temperatures, the former covers more areas near and above the phase envelope. Thus, benzene + water should just have a slightly less delayed mixing than water + naphthalene, which is consistent with the normalized water diffusion time presented in Fig. 6.
2) Water + naphthalene mixture (Fig. 7b) exhibits the widest non-ideal region amongst the four mixtures discussed here. This can be explained by its phase behavior: (i) The *Tx* projection of the critical locus starting from the water critical point shown in Figs. 2 and 7b covers the entire *x*-coordinate. It causes a larger (cyan) region of $\tilde{d} \approx 0$ above the phase envelope, and causes the expansion of the non-ideal (yellow and orange) region towards $x = 0$. (ii) The projection of the LL critical locus of this system starting from the upper critical end-point (UCEP) has the least slope in the *PT* plane (Fig. 2). This effect appears as an orange region in Fig. 7b at $T > 560$ K and $x_W \in (0.6,0.8)$, while at lower temperatures, both effects seem superposed.
3) Water + *n*-decane system (Fig. 7c) has a short range between its UCST at 24 MPa and the water critical temperature. Its critical locus starting at the water critical point is limited within $0.9 \leq x \leq 1$ before diverging to high pressures. Accordingly, the non-ideal region projected by this branch is small. Nonetheless, the branch of this critical locus that diverges to high pressures seems to influence the middle composition region around 650 K. Moreover, the critical locus starting from *n*-decane critical point begins at a lower temperature, and expands from $x = 0$ up to the UCEP. Thus, the non-ideal region grows to a wide range both in temperature and mole fraction. Especially, the colors from orange to yellow cover the nearby regions above the phase envelope. Furthermore, the water composition in the mixture at the UCST is richer than previous binaries. Therefore, there is no jump in the mixing time for this binary system. As a result, the overall non-ideal effect is relatively strong but weaker than water + benzene, and water + naphthalene.
4) Water + *n*-triacontane system (Fig. 7d) exhibits the highest UCST at 24 MPa. It is the most size-asymmetrical system in this study. In contrast with the previous systems, the critical locus starting from the critical point of water ends at an UCEP that is very close to the water critical point. On the other hand, the critical locus starting from *n*-triacontane critical point covers a wide range of temperatures, from 660 K up to the pure HC critical point; however, at the lower temperatures, it covers a very small range of water mole fraction ($0.88 \leq x \leq 0.95$). Consequently, the non-ideal region is very limited: $\tilde{d} \approx 1$ up to a water mole fraction of 0.6, while the non-

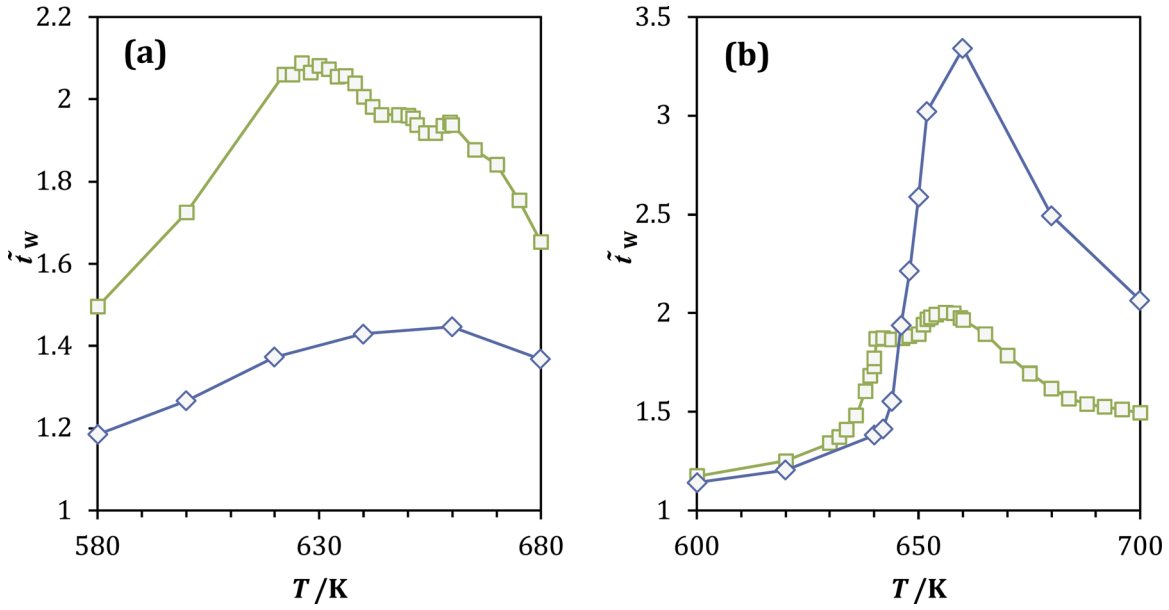

Fig. 8. Normalized mixing time, $\tilde{t}_W$, for (a) *n*-decane and (b) 1-decylnaphthalene. Symbols: Simulation results obtained using either (□) GCA-EOS (this work) or (◇) PR-EOS (He et al. [26]). Solid lines included to help visualization.

ideal region starts at $x = 0.8$. As a result, water diffusion into the droplet should be delayed mostly during the last moments of mixing.

Results shown so far have depicted how the phase equilibria, both mutual solubilities and critical loci, may influence to an appreciable extent the mixing process. Thus, the analysis of the global phase behavior of these systems could provide clues regarding these effects. As shown in Figs. 2 and 3, three phase behavior types have been predicted by the GCA-EOS, which are consistent with experimental data in the literature. These types are Type II for water + naphthalene, Type IIIa for water + benzene or + *n*-decane, and Type IIIb for water + *n*-triacontane. Our study shows that Type II and Type IIIa have similar behaviors regarding non-ideal diffusion: (1) The lower the UCST is, the stronger non-ideal diffusion is exhibited; and (2) the wider the critical locus expands in the mole fraction of water, the stronger non-ideal diffusion is exhibited. Our results show that Type IIIb behaves differently from the previous types: The non-ideal region is limited to high temperatures and large water mole fractions. As a result, the non-ideal diffusion of Type IIIb is weak.

4.2.3. Comparison between different EOS predictions

The departure coefficient of the diffusion driving force not only facilitates the interpretation of the simulation results, it also helps explain the impact of the thermodynamic model chosen to assess the non-ideal driving forces. As mentioned previously, He et al. [26] performed simulations using PR-EOS, while in this work the GCA-EOS is used. The simulation results obtained here are qualitatively similar; both models predict the effect of the mixture non-ideality. This is expected, as both EOSs predict similar critical loci near our simulation conditions. Nonetheless, the extent of this effect is rather different for both models. For example, Fig. 8 compares the normalized mixing times using either GCA- or PR-EOSs, for *n*-decane and 1-decylnaphthalene. The simulations using the GCA-EOS predict a 50% higher mixing times for *n*-decane, while 60% smaller for 1-decylnaphthalene. Although both models reproduce close water solubilities in *n*-decane of Haruki et al. [57], they predict different values of the fugacity coefficient derivatives. Moreover, the *Tx* projections of the critical lines shown in Fig. 9 seems similar for both models. Nonetheless, the *PT* projection depicted in Fig. 10 shows that the two models predict rather different pressures along the critical lines, and that the GCA-EOS result with parameters from this work is closer to the experimental data of Brunner [58]. It is worth mentioning that this work is not an evaluation to conclude which model is better, but to compare different parameterizations. Note that

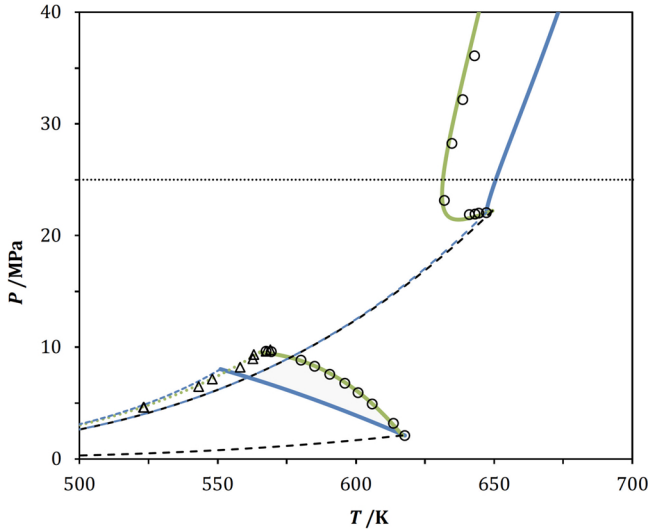

Fig. 10. Comparison of the *PT* projection of the global phase equilibria for GCA-EOS (green lines) and PR-EOS (blue lines) [26] for water + *n*-decane. Symbols: experimental data [58]. Lines: GCA-EOS prediction of: (- - -) pure vapor pressures, (—) critical loci, and (· · ·) three phase line. (For interpretation of the references to colour in this figure legend, the reader is referred to the web version of this article).

the mismatch of mixing times as well as diffusion driving forces between the two EOSs is caused by the mismatch of the first-order derivatives of fugacities as revealed in the *PT* projections, even though the fugacities themselves are closely predicted by the two EOSs as shown in the solubilities and *Tx* projections. This research reveals the importance of the accuracy of the first-order derivatives of EOS in predicting the non-ideal diffusion process.

From Figs. 9 and 10, it seems clear that the reproduction of mutual solubility is not a complete approach to produce quantitative results when simulating at conditions near a critical point. Similarly, Fig. 11 shows the contour chart for 1-decylnaphthalene calculated using either GCA- or PR-EOSs. In this case, the extent of the non-ideal region is larger for PR-EOS than GCA, which then manifests in larger mixing times. Furthermore, Fig. 12 shows that the GCA-EOS predicts a close transition from Types IIIa towards IIIb, as the UCEP is close to the critical line starting from water critical point. Therefore, the GCA-EOS predicts that the behavior of water + 1-decylnaphthalene is more

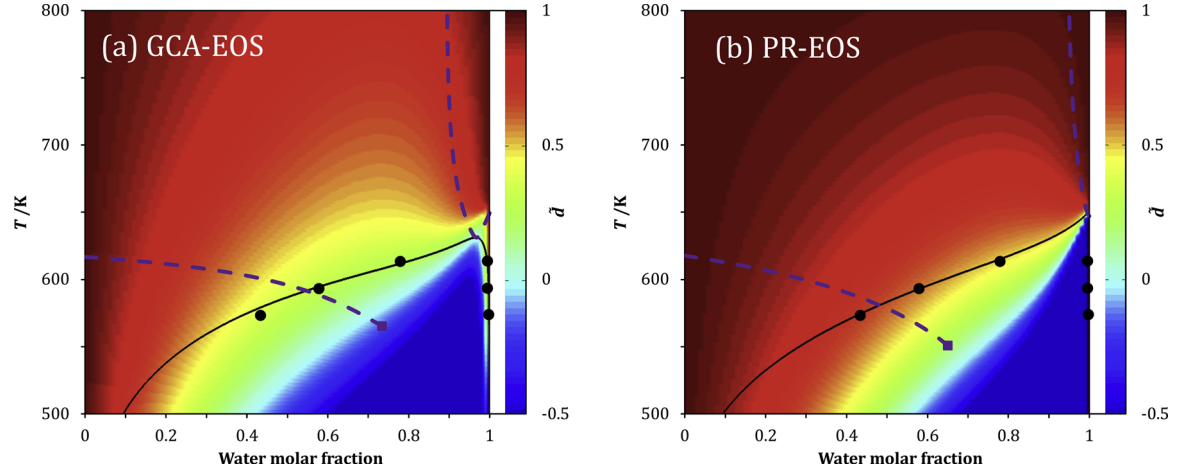

Fig. 9. Coefficient of driving force ($\tilde{d}$) comparison for water + *n*-decane system between (a) GCA-EOS and (b) PR-EOS. Black circles: experimental mutual solubility data [57]. Black solid lines: mutual solubility at 24 MPa calculated with the GCA-EOS. Thick violet dashed line: *Tx* projection of the critical loci calculated for each thermodynamic model; violet square: predicted critical end-point. (For interpretation of the references to color in this figure, the reader is referred to the electronic version of this article.).

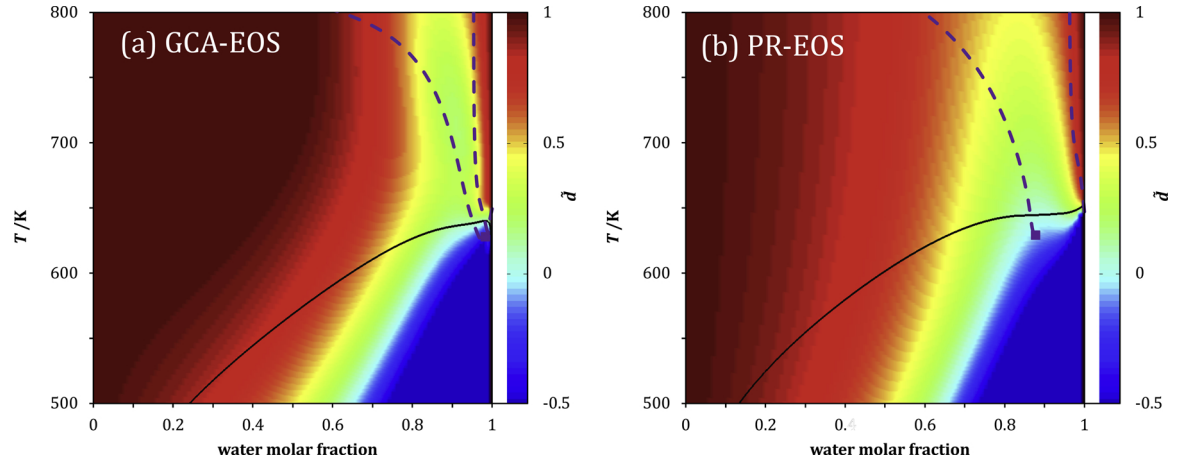

Fig. 11. Coefficient of driving force ($\tilde{d}$) comparison for 1-decylnaphthalene between (a) GCA-EOS and (b) PR-EOS. Black lines: mutual solubility at 24 MPa calculated with the GCA-EOS. Thick violet dashed line: *Tx* projection of the critical loci calculated for each thermodynamic model; violet square: predicted critical end-point. (For interpretation of the references to color in this figure, the reader is referred to the electronic version of this article).

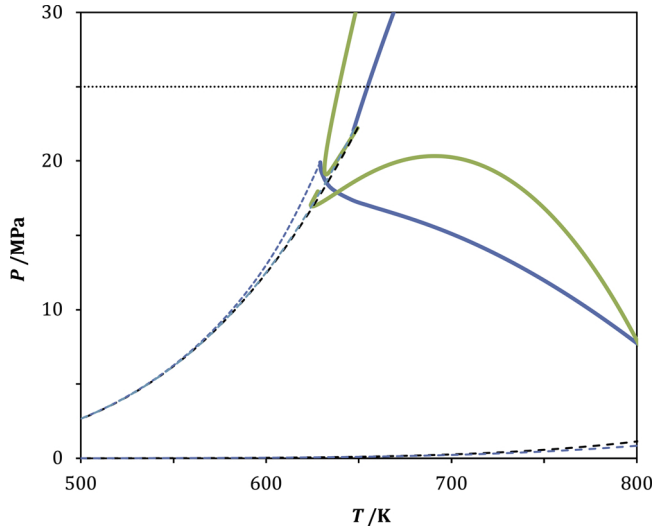

Fig. 12. Comparison of the *PT* projection of the global phase equilibria for GCA-EOS (green) and PR-EOS (blue) for water + 1-decylnaphthalene system. Lines: GCA-EOS prediction of: (- - -) pure vapor pressures, (—) critical loci, and (· · ·) three phase line. (For interpretation of the references to colour in this figure legend, the reader is referred to the web version of this article).

similar to water + *n*-triacontane (i.e., highly size asymmetrical), whose ideal region ($\tilde{d} \approx 1$) is large as shown in Figs. 7d and 11a.

5. Conclusions

Because of the strong coupling of thermodynamics, transport phenomena, and chemical kinetics in SCF processes, modeling their dynamics and mixing has been the subject of a sustained effort. In this work, the mixing of model hydrocarbons in NCW and SCW is studied at constant pressure using the GCA-EOS. This work includes *n*-decane, *n*-triacontane, benzene, naphthalene and 1-decylnaphthalene as model compounds. The effect of the non-ideality of the mixture over the diffusion driving force is studied, with emphasis on the description of the chemical potential near the critical point. To do so, the H_2O + alkyl group binary interaction parameters were revisited to properly describe mutual solubility of alkanes and mixture critical points near the temperature and pressure ranges of interest.

Similar to our previous work using a different EOS, simulation results show that using the non-ideal driving force, the mixing is significantly delayed by factor of 1.6 to 2.4 for the systems under study. Based on the predicted conditions of the binary mixture critical point, it is shown that this is a natural result, as the non-ideal driving force is proportional to composition derivatives of the chemical potential, which is null at the critical point. This effect was analyzed using the departure coefficient of the driving force. This analysis show that the delayed mixing is marked not only for the mixture UCST at a specified pressure, but also other critical points close to the simulation conditions. Therefore, the correct description of the critical loci of the mixture is important to achieve reliable simulations. Moreover, comparison between the results from previous work using the PR-EOS and those from the current work using GCA-EOS, shows that even if the mutual solubility is correctly reproduced, it may produce different predictions of the critical loci and hence the driving force is affected quantitatively. Therefore, to predict accurate mixing processes, the selection and parameterization of a thermodynamic model should reproduce *both* the equilibrium compositions and critical loci measured in experiments.

Acknowledgments

F.A. Sánchez and S. Pereda acknowledge the financial support granted by the Consejo Nacional de Investigaciones Científicas y Técnicas (CONICET- PIP 11220110100454 / PIP 11220150100856 CO), the Secretaría de Ciencia, Tecnología e Innovación Productiva (MinCyT PICT 2012/1998 / PICT 2014/2293), and Universidad Nacional del Sur (UNS - 24/M133). Ping He and Ahmed Ghoniem acknowledge the support through a Research Agreement with Saudi Aramco, a Founding Member of the MIT Energy Initiative, (contract number 6600023444). Ping He acknowledges the Research Enhancement Grant (2018) Award, Center for Innovation, Commercialization and Entrepreneurship (CICE), Center for Advances in Port Management, at LU for supporting this research. Ping He thanks Mr. Paul G. Latiolais for discussions and encouragement.

Appendix A. The GCAGCA-EOS mathematical model

There are three contributions to the residual Helmholtz energy in the GCAare three contributions to the residual Helmholtz energy in the GCA-EOS model: free volume, attractive and associating. The free volume and attractive contributions keep the same form as the original GC-EOS [42].

The Carnahan–Starling repulsive term follows the expression developed by Mansoori and Leland [60]:

$$\frac{A^{fv}}{R\,T} = \frac{\lambda_1\lambda_2}{\lambda_3}(Y-1) + \frac{\lambda_2^3}{\lambda_3^2}(Y^2 - Y - \ln Y) + n\,\ln Y \tag{A.1}$$

where

$$Y = \left(1 - \frac{\pi\,\lambda_3}{6\,V}\right)^{-1} \tag{A.2}$$

$$\lambda_k = \sum_{i=1}^{NC} n_i d_i^k (k = 1,\ 2,\ 3) \tag{A.3}$$

where n_i is the number of moles of component i, NC stands for the number of components, V represents the total volume, R stands for universal gas constant and T is temperature.

The following generalized expression is assumed for the hard sphere diameter temperature dependence:

$$d_i = 1.065655\,d_{ci}\left[1 - 0.12\exp\left(\frac{-2\,T_{ci}}{3\,T}\right)\right] \tag{A.4}$$

where d_c is the value of the hard sphere diameter at the critical temperature, T_c, for the i-th component.

The attractive contribution to the residual Helmholtz energy (A^{att}) accounts for dispersive forces between functional groups. It is a van der Waals type contribution combined with a density-dependent, local-composition expression based on a group contribution version of the NRTL model [61]. Integrating van der Waals EoS, $A^{att}(T,V)$ is equal to $-a{\cdot}n{\cdot}\rho$ being a the energy parameter, n the number of moles and ρ the mol density. For a pure component a is computed as follows:

$$a = \frac{z}{2}q^2 g \tag{A.5}$$

where g is the characteristic attractive energy per segment and q is the surface segment area per mole as defined in the UNIFAC method [62]. The interactions are assumed to take place through the surface and the coordination number z is set equal 10 as usual. In GCA-EOS the extension to mixtures is carried out using the two fluids model NRTL model, but using local surface fractions like in UNIQUAC [45] rather than local mole fractions. Therefore, the A^{att} for the mixture becomes

$$\frac{A^{att}}{R\,T} = -\frac{\frac{z}{2}\tilde{q}^2\,g_{mix}}{R\,T\,V} \tag{A.6}$$

where $\tilde{q}$ is the total number of surface segments and g_{mix} the mixture characteristic attractive energy per total segments and are calculated as follows:

$$g_{mix} = \sum_{i=1}^{NG}\theta_i \sum_{j=1}^{NG}\frac{\theta_j\tau_{ji}g_{ji}}{\sum_{k=1}^{NG}\theta_k\tau_{ki}} \tag{A.7}$$

and

$$\tilde{q} = \sum_{i=1}^{NC}\sum_{j=1}^{NG} n_i\nu_{ij}q_j \tag{A.8}$$

where ν_{ij} is the number of groups of type j in molecule i; q_j stands for the number of surface segments assigned to group j; θ_j represents the surface fraction of group j;

$$\theta_j = \frac{1}{\tilde{q}}\sum_{i=1}^{NC} n_i\nu_{ij}q_j \tag{A.9}$$

$$\tau_{ji} = \exp\left(\alpha_{ji}\frac{\tilde{q}\,\Delta g_{ji}}{R\,T\,V}\right) \tag{A.10}$$

$$\Delta g_{ij} = g_{ij} - g_{jj} \tag{A.11}$$

g_{ji} stands for the attractive energy between groups i and j; and α_{ji} is the non-randomness parameter. The attractive energy between unlike groups is calculated from the corresponding interactions between like groups:

$$g_{ij} = k_{ij}\sqrt{g_{ii}g_{jj}}\ (k_{ij} = k_{ji}) \tag{A.12}$$

with the following temperature dependence for the energy and interaction parameters:

$$g_{ii} = g_{ii}^*[1 + g_{ii}'(\frac{T}{T_i^*} - 1) + g_{ii}'\ln(\frac{T}{T_i^*})] \tag{A.13}$$

and

$$k_{ij} = k_{ij}^*\left[1 + k_{ij}'\ln\left(\frac{2\,T}{T_i^* + T_j^*}\right)\right] \tag{A.14}$$

where g_{ii}^* is the attractive energy and k_{ij}^* the interaction parameter at the reference temperature T_i^* and $(T_i^* + T_j^*)/2$, respectively.

The associating term A^{assoc} follows SAFT equation through a group-contribution expression [63]:

$$\frac{A^{assoc}}{R\,T} = \sum_{i=1}^{NGA} n_i^* \left[\sum_{k=1}^{M_i} \left(\ln X_{ki} - \frac{X_{ki}}{2} \right) + \frac{M_i}{2} \right] \tag{A.15}$$

In this equation *NGA* represents the number of associating functional groups, n_i^* the total number of moles of associating group *i*, X_{ki} the fraction of group *i* non-bonded through site *k* and M_i the number of associating sites in group *i*. The total number of moles of associating group *i* is calculated from the number ν_{mi}^* of associating groups *i* present in molecule *m* and the total amount of moles of specie *m* (n_m):

$$n_i^* = \sum_{m=1}^{NC} \nu_{mi}^* n_m \tag{A.16}$$

The fraction of groups *i* non-bonded through site *k* is determined by the expression:

$$X_{ki} = \left(1 + \sum_{j=1}^{NGA} \sum_{l=1}^{M_j} \frac{n_j^* X_{lj} \Delta_{ki,lj}}{V} \right)^{-1} \tag{A.17}$$

where the summation includes all *NGA* associating groups and M_j sites. X_{ki} depends on the on the association strength $\Delta_{ki,lj}$:

$$\Delta_{ki,lj} = \kappa_{ki,lj} \left[\exp\left(\frac{\varepsilon_{ki,lj}}{R\,T} \right) - 1 \right] \tag{A.18}$$

The association strength between site *k* of group *i* and site *l* of group *j* depends on the temperature *T* and on the association parameters $\kappa_{ki,jl}$ and $\varepsilon_{ki,jl}$, which represent the volume and energy of association, respectively. Thermodynamic properties for evaluating phase equilibria may be derived from the residual Helmholtz free energy (Eq. 14), following Maxwell relations.

Appendix B. GCA-EOS parameters used in this work

This Appendix reports all the GCA-EOS parameters required to model the system under study. Tables B1 and B2 summarize those of the attractive contribution (pure group surface energy and binary interaction), while Table B3 lists parameters for the association interactions (association energy and volume). In each case we also include the source of the parameters taken from previous works. In contrast, for those parameters fitted in this work, we indicate the correlated experimental data in the table footnotes. On the other hand, Table B4 reports properties of all the compounds evaluated in this work: group assembly, and the parameters for the repulsive contribution (critical diameter and critical temperature).

Table B1
Pure group parameters for the attractive term of the GCA-EOS.

Group	T^*/K	q	g^*/(atm cm^6 mol^{-2})	g'	g''	Reference
CH_3	600	0.848	316910	−0.9274	0	[42]
CH_2	600	0.540	356080	−0.8755	0	[42]
ACH	600	0.40	723210	−0.6060	0	[42]
AC	600	0.285	723210	−0.6060	0	[42]
$ACCH_2$	600	0.660	506290	−0.8013	0	[42]
H_2O	647.13	0.866	964720	−1.2379	1.0084	[52]

Table B2
Binary interaction parameters used in this work.

Group		k_{ij}^*	k_{ij}'	α_{ij}	α_{ji}	Reference
i	j					
H_2O	CH_3^∞	0.6723	−0.055	−7.704	0.691	This work[a]
	CH_2^∞	0.5013	−0.075	−4.549	8.218	This work[a]
	ACH^∞/AC^∞	0.9100	−0.056	2.0	4.0	[29]
	$ACCH_2^\infty$	1.1500	0	0	0	[29]
CH_3/CH_2	ACH/AC	1.0410	0.0944	0.3915	0.3915	[42]

[a] High pressure VLE and LLE of water + *n*-dodecane [56], and water solubility in *n*-hexadecane and *n*-eicosane [57].

Table B3
Self and cross-associating parameters of GCA-EOS correlated in this work.

Site *k*	Group *i*	Site *l*	Group *j*	$\varepsilon_{ki,lj}\,R^{-1}$ /K	$\kappa_{ki,lj}$ /(cm^3 mol^{-1})	Reference
(–)	Arom. Ring	(+)	H_2O	1760	0.2300	[29]
(–)	H_2O	(+)	H_2O	2350	0.3787	[52]

Table B4
Pure compound critical temperatures and diameters for the free-volume contribution of GCA-EOS.

Compound	T_c /K	d_c /(cm mol$^{-1/3}$)[a]	Group assembly	Ref.
water	647.13	2.5763[b]	H_2O	[52]
n-decane	617.70	6.0051	$2\times CH_3 + 8\times CH_2$	[39]
n-dodecane	658.00	6.4480	$2\times CH_3 + 10\times CH_2$	[39]
n-hexadecane	723.00	7.2391	$2\times CH_3 + 14\times CH_2$	[39]
n-triacontane	850.00	9.2462[b]	$2\times CH_3 + 28\times CH_2$	[58]
benzene	562.00	4.3813	$6\times$ ACH	[39]
naphthalene	748.00	5.1646	$8\times$ ACH + 2 × AC	[39]
1-decylnaphthalene	859.00	7.3726	$CH_3 + 8\times CH_2 + 7\times$ ACH + 2 × AC + $ACCH_2$	[39]

[a] Unless noticed, the critical diameter is calculated to match a saturation point.
[b] Critical diameter obtained from the critical constraints.

References

[1] C.F. Curtiss, R.B. Bird, Multicomponent diffusion, Ind. Eng. Chem. Res. 38 (1999) 2515–2522, https://doi.org/10.1021/ie9901123.
[2] G.L. Standart, R. Taylor, R. Krishna, The Maxwell-Stefan formulation of irreversible thermodynamics for simultaneous heat and mass transfer, Chem. Eng. Commun. 3 (1979) 277–289, https://doi.org/10.1080/00986447908935866.
[3] R.B. Bird, D.J. Klingenberg, Multicomponent diffusion—a brief review, Adv. Water Resour. 62 (Part B) (2013) 238–242, https://doi.org/10.1016/j.advwatres.2013.05.010.
[4] J.O. Hirschfelder, C.F. Curtiss, R.B. Bird, The Molecular Theory of Gases and Liquids, 1st ed., Wiley, New York, NY, 1964.
[5] J.S. Shuen, V. Yang, C.C. Hsiao, Combustion of liquid-fuel droplets in supercritical conditions, Combust. Flame 89 (1992) 299–319, https://doi.org/10.1016/0010-2180(92)90017-J.
[6] V. Yang, Modeling of supercritical vaporization, mixing, and combustion processes in liquid-fueled propulsion systems, Proc. Combust. Inst. 28 (2000) 925–942, https://doi.org/10.1016/S0082-0784(00)80299-4.
[7] K.S. Lieball, Numerical investigations on a transpiring wall reactor for supercritical water oxidation, ETH Zürich (2003), https://doi.org/10.3929/ethz-a-004495126.
[8] T. Fadli, A. Erriguible, S. Laugier, P. Subra-Paternault, Simulation of heat and mass transfer of CO2–solvent mixtures in miscible conditions: isothermal and non-isothermal mixing, J. Supercrit. Fluids 52 (2010) 193–202, https://doi.org/10.1016/j.supflu.2010.01.008.
[9] G.C. Hsiao, H. Meng, V. Yang, Pressure-coupled vaporization response of n-pentane fuel droplet at subcritical and supercritical conditions, Proc. Combust. Inst. 33 (2011) 1997–2003, https://doi.org/10.1016/j.proci.2010.06.049.
[10] S. Dabiri, G. Wu, M.T. Timko, A.F. Ghoniem, Mixing of single-component hydrocarbon droplets and water at supercritical or near-critical conditions, J. Supercrit. Fluids 67 (2012) 29–40, https://doi.org/10.1016/j.supflu.2012.02.014.
[11] G. Wu, S. Dabiri, M.T. Timko, A.F. Ghoniem, Fractionation of multi-component hydrocarbon droplets in water at supercritical or near-critical conditions, J. Supercrit. Fluids 72 (2012) 150–160, https://doi.org/10.1016/j.supflu.2012.08.021.
[12] A. Raghavan, A.F. Ghoniem, Simulation of supercritical water–hydrocarbon mixing in a cylindrical tee at intermediate Reynolds number: formulation, numerical method and laminar mixing, J. Supercrit. Fluids 92 (2014) 31–46, https://doi.org/10.1016/j.supflu.2014.04.015.
[13] A. Raghavan, A.F. Ghoniem, Simulation of supercritical water–hydrocarbon mixing in a cylindrical tee at intermediate Reynolds number: impact of temperature difference between streams, J. Supercrit. Fluids 95 (2014) 325–338, https://doi.org/10.1016/j.supflu.2014.09.030.
[14] C. Narayanan, C. Frouzakis, K. Boulouchos, K. Príkopský, B. Wellig, P. Rudolf von Rohr, Numerical modelling of a supercritical water oxidation reactor containing a hydrothermal flame, J. Supercrit. Fluids 46 (2008) 149–155, https://doi.org/10.1016/j.supflu.2008.04.005.
[15] J. Sierra-Pallares, M. Teresa Parra-Santos, J. García-Serna, F. Castro, M. José Cocero, Numerical modelling of hydrothermal flames. Micromixing effects over turbulent reaction rates, J. Supercrit. Fluids 50 (2009) 146–154, https://doi.org/10.1016/j.supflu.2009.05.001.
[16] J. Sierra-Pallares, D.L. Marchisio, E. Alonso, M.T. Parra-Santos, F. Castro, M. José Cocero, Quantification of mixing efficiency in turbulent supercritical water hydrothermal reactors, Chem. Eng. Sci. 66 (2011) 1576–1589, https://doi.org/10.1016/j.ces.2010.12.039.
[17] J.O. Werling, P.G. Debenedetti, Numerical modeling of mass transfer in the supercritical antisolvent process, J. Supercrit. Fluids 16 (1999) 167–181, https://doi.org/10.1016/S0896-8446(99)00027-3.
[18] J.O. Werling, P.G. Debenedetti, Numerical modeling of mass transfer in the supercritical antisolvent process: miscible conditions, J. Supercrit. Fluids 18 (2000) 11–24, https://doi.org/10.1016/S0896-8446(00)00054-1.
[19] J. Bellan, Theory, modeling and analysis of turbulent supercritical mixing, Combust. Sci. Technol. 178 (2006) 253–281, https://doi.org/10.1080/00102200500292241.
[20] K. Harstad, J. Bellan, Interactions of fluid oxygen drops in fluid hydrogen at rocket chamber pressures, Int. J. Heat Mass Transf. 41 (1998) 3551–3558, https://doi.org/10.1016/S0017-9310(98)00048-9.
[21] K. Harstad, J. Bellan, Isolated fluid oxygen drop behavior in fluid hydrogen at rocket chamber pressures, Int. J. Heat Mass Transf. 41 (1998) 3537–3550, https://doi.org/10.1016/S0017-9310(98)00049-0.
[22] K. Harstad, J. Bellan, The Lewis number under supercritical conditions, Int. J. Heat Mass Transf. 42 (1999) 961–970, https://doi.org/10.1016/S0017-9310(98)00230-0.
[23] R.S. Miller, K.G. Harstad, J. Bellan, Direct numerical simulations of supercritical fluid mixing layers applied to heptane–nitrogen, J. Fluid Mech. 436 (2001) 1–39, https://doi.org/10.1017/S0022112001003895.
[24] E. Peacock-López, L. Woodhouse, Generalized transport theory and its application to binary mixtures, in: E. Matteoli, G.A. Mansoori (Eds.), Fluct. Theory Mix. 1st ed., Taylor & Francis, 1990, pp. 301–333.
[25] M.T. Timko, A.F. Ghoniem, W.H. Green, Upgrading and desulfurization of heavy oils by supercritical water, J. Supercrit. Fluids 96 (2015) 114–123, https://doi.org/10.1016/j.supflu.2014.09.015.
[26] P. He, A. Raghavan, A.F. Ghoniem, Impact of non-ideality on mixing of hydrocarbons and water at supercritical or near-critical conditions, J. Supercrit. Fluids 102 (2015) 50–65, https://doi.org/10.1016/j.supflu.2015.03.017.
[27] P. He, A.F. Ghoniem, Phase separation during mixing of partially miscible fluids under near-critical and supercritical conditions, and the phenomenon of uphill diffusion, J. Supercrit. Fluids 135 (2018) 105–119, https://doi.org/10.1016/j.supflu.2017.12.040.
[28] H.P. Gros, S.B. Bottini, E.A. Brignole, A group contribution equation of state for associating mixtures, Fluid Phase Equilib. 116 (1996) 537–544, https://doi.org/10.1016/0378-3812(95)02928-1.
[29] F.A. Sánchez, S. Pereda, E.A. Brignole, GCA-EoS: a SAFT group contribution model—extension to mixtures containing aromatic hydrocarbons and associating compounds, Fluid Phase Equilib. 306 (2011) 112–123 (Accessed 17 September 2013), http://www.sciencedirect.com/science/article/pii/S0378381211001646.
[30] F.A. Sánchez, Ingeniería de Equilibrio de Fases en Biorrefinerías (Phase Equilibrium Engineering in Biorefineries), Ph. D. Thesis Universidad Nacional del Sur, 2013, http://repositoriodigital.uns.edu.ar/handle/123456789/2459.
[31] P.H. van Konynenburg, R.L. Scott, Critical lines and phase equilibria in binary van der waals mixtures, Philos. Trans. R. Soc. A Math. Phys. Eng. Sci. 298 (1980) 495–540, https://doi.org/10.1098/rsta.1980.0266.
[32] P. He, A.F. Ghoniem, A sharp interface method for coupling multiphase flow, heat transfer and multicomponent mass transfer with interphase diffusion, J. Comput. Phys. 332 (2017) 316–332, https://doi.org/10.1016/j.jcp.2016.12.002.
[33] M. Watanabe, S. Kato, S. Ishizeki, H. Inomata, R.L. Smith, Heavy oil upgrading in the presence of high density water: basic study, J. Supercrit. Fluids 53 (2010) 48–52, https://doi.org/10.1016/j.supflu.2009.11.013.
[34] T. Sato, Upgrading of heavy oil by hydrogenation through partial oxidation and water-gas shift reaction in supercritical water, J. Japan Pet. Inst. 57 (2014) 1–10, https://doi.org/10.1627/jpi.57.1.
[35] X.-C. Tan, Q.-K. Liu, D.-Q. Zhu, P.-Q. Yuan, Z.-M. Cheng, W.-K. Yuan, Pyrolysis of heavy oil in the presence of supercritical water: the reaction kinetics in different phases, AIChE J. 61 (2015) 857–866, https://doi.org/10.1002/aic.14677.
[36] Q.-K. Liu, D.-Q. Zhu, X.-C. Tan, P.-Q. Yuan, Z.-M. Cheng, W.-K. Yuan, J.-Y. Yang, Lumped reaction kinetic models for pyrolysis of heavy oil in the presence of supercritical water, AIChE J. 62 (2016) 207–216, https://doi.org/10.1002/aic.14978.
[37] P. Blanco, M.M. Bou-Ali, J.K. Platten, D.A. de Mezquia, J.A. Madariaga, C. Santamaría, Thermodiffusion coefficients of binary and ternary hydrocarbon mixtures, J. Chem. Phys. 132 (2010) 114506, , https://doi.org/10.1063/1.3354114.
[38] P. Blanco, M. Mounir Bou-Ali, J.K. Platten, P. Urteaga, J.A. Madariaga, C. Santamaria, Determination of thermal diffusion coefficient in equimolar n-alkane mixtures: empirical correlations, J. Chem. Phys. 129 (2008) 174504, , https://doi.org/10.1063/1.2945901.
[39] H. Liu, C.M. Silva, E.A. Macedo, New equations for tracer diffusion coefficients of solutes in supercritical and liquid solvents based on the lennard-jones fluid model, Ind. Eng. Chem. Res. 36 (1997) 246–252, https://doi.org/10.1021/ie9602318.
[40] J.A. Wesselingh, R. Krishna, Mass Transfer, 1st ed., E. Horwood, 1990, https://books.google.com.ar/books?id=WrZTAAAAMAAJ.

[41] T.H. Chung, M. Ajlan, L.L. Lee, K.E. Starling, Generalized multiparameter correlation for nonpolar and polar fluid transport properties, Ind. Eng. Chem. Res. 27 (1988) 671–679, https://doi.org/10.1021/ie00076a024.
[42] S. Skjold-jørgensen, Group contribution equation of state (GC-EOS): a predictive method for phase equilibrium computations over wide ranges of temperature and pressures up to 30 MPa, Ind. Eng. Chem. Res. 27 (1988) 110–118.
[43] N.F. Carnahan, K.E. Starling, Equation of state for nonattracting rigid spheres, J. Chem. Phys. 51 (1969) 635, https://doi.org/10.1063/1.1672048.
[44] G.A. Mansoori, N.F. Carnahan, K.E. Starling, T.W. Leland Jr, Equilibrium thermodynamic properties of the mixture of hard spheres, J. Chem. Phys. 54 (1971) 1523–1525, https://doi.org/10.1063/1.1675048.
[45] D.S. Abrams, J.M. Prausnitz, Statistical thermodynamics of liquid mixtures: a new expression for the excess Gibbs energy of partly or completely miscible systems, AIChE J. 21 (1975) 116–128, https://doi.org/10.1002/aic.690210115.
[46] W.G. Chapman, K.E. Gubbins, G. Jackson, M. Radosz, SAFT: equation-of-state solution model for associating fluids, Fluid Phase Equilib. 52 (1989) 31–38, https://doi.org/10.1016/0378-3812(89)80308-5.
[47] A. Bondi, van der Waals, Volumes and radii, J. Phys. Chem. 68 (1964) 441–451, https://doi.org/10.1021/j100785a001.
[48] F.A. Sánchez, S. Pereda, E.A. Brignole, GCA-EoS: a SAFT group contribution model—extension to mixtures containing aromatic hydrocarbons and associating compounds, Fluid Phase Equilib. 306 (2011) 112–123, https://doi.org/10.1016/j.fluid.2011.03.024.
[49] M. González Prieto, F.A. Sánchez, S. Pereda, Thermodynamic model for biomass processing in pressure intensified technologies, J. Supercrit. Fluids 96 (2015) 53–67, https://doi.org/10.1016/j.supflu.2014.08.024.
[50] M. Cismondi Duarte, M.L. Michelsen, Global phase equilibrium calculations: critical lines, critical end points and liquid–liquid–vapour equilibrium in binary mixtures, J. Supercrit. Fluids 39 (2007) 287–295, https://doi.org/10.1016/j.supflu.2006.03.011.
[51] S. Skjold-Jørgensen, Group contribution equation of state (GC-EOS): a predictive method for phase equilibrium computations over wide ranges of temperature and pressures up to 30 MPa, Ind. Eng. Chem. Res. 27 (1988) 110–118, https://doi.org/10.1021/ie00073a021.
[52] T.M. Soria, F.A. Sánchez, S. Pereda, S.B. Bottini, Modeling alcohol + water + hydrocarbon mixtures with the group contribution with association equation of state GCA-EoS, Fluid Phase Equilib. 296 (2010) 116–124, https://doi.org/10.1016/j.fluid.2010.02.040.
[53] E. Brunner, M.C. Thies, G.M. Schneider, Fluid mixtures at high pressures: phase behavior and critical phenomena for binary mixtures of water with aromatic hydrocarbons, J. Supercrit. Fluids 39 (2006) 160–173, https://doi.org/10.1016/j.supflu.2005.12.003.
[54] M.L. Michelsen, The isothermal flash problem. Part I. Stability, Fluid Phase Equilib. 9 (1982) 1–19, https://doi.org/10.1016/0378-3812(82)85001-2.
[55] M.L. Michelsen, The isothermal flash problem. Part II. Phase-split calculation, Fluid Phase Equilib. 9 (1982) 21–40, https://doi.org/10.1016/0378-3812(82)85002-4.
[56] R.L. Stevenson, D.S. LaBracio, T.A. Beaton, M.C. Thies, Fluid Phase Equilibria and critical phenomena for the dodecane-water and squalane-water systems at elevated temperatures and pressures, Fluid Phase Equilib. 93 (1994) 317–336, https://doi.org/10.1016/0378-3812(94)87016-0.
[57] M. Haruki, Y. Iwai, S. Nagao, Y. Yahiro, Y. Arai, Measurement and correlation of phase equilibria for water + hydrocarbon systems near the critical temperature and pressure of water, Ind. Eng. Chem. Res. 39 (2000) 4516–4520, https://doi.org/10.1021/ie000185i.
[58] E. Brunner, Fluid mixtures at high pressures IX. Phase separation and critical phenomena in 23 (n-alkane + water) mixtures, J. Chem. Thermodyn. 22 (1990) 335–353, https://doi.org/10.1016/0021-9614(90)90120-F.
[59] A. Firoozabadi, Equilibrium, stability, and criticality, Thermodyn. Hydrocarb. Reserv. 1st ed., McGraw Hill, New York, NY, 1999, pp. 260–264.
[60] G.A. Mansoori, N.F. Carnahan, K.E. Starling, T.W. Leland, Equilibrium thermodynamic properties of the mixture of hard spheres, J. Chem. Phys. 54 (1971) 1523–1525, https://doi.org/10.1063/1.1675048.
[61] H. Renon, J.M. Prausnitz, Local compositions in thermodynamic excess functions for liquid mixtures, AIChE J. 14 (1968) 135–144, https://doi.org/10.1002/aic.690140124.
[62] Å. Fredenslund, J. Gmehling, P. Rasmussen, Vapor-liquid equilibria using UNIFAC, in: H. Renon (Ed.), A Group Contribution Method, 1st ed., Elsevier Ltd, Amsterdam, 1977, pp. 27–64, , https://doi.org/10.1016/0378-3812(77)80014-9 Fluid Phase Equilib..
[63] H.P. Gros, S.B. Bottini, E.A. Brignole, A group contribution equation of state for associating mixtures, Fluid Phase Equilib. 116 (1996) 537–544, https://doi.org/10.1016/0378-3812(95)02928-1.